UC Berkeley
UC Berkeley Previously Published Works

Title

Synthesis and Characterization of Supported Cobalt–Manganese Nanoparticles as Model Catalysts for Fischer–Tropsch Synthesis

Permalink

https://escholarship.org/uc/item/9zb4p8sg

Journal

ChemCatChem, 6(10)

ISSN

1867-3880

Authors

Werner, Sebastian
Johnson, Gregory R
Bell, Alexis T

Publication Date

2014-10-01

DOI

10.1002/cctc.201402260

Peer reviewed

Synthesis and Characterization of Supported Cobalt–Manganese Nanoparticles as Model Catalysts for Fischer–Tropsch Synthesis

Sebastian Werner, Gregory R. Johnson, and Alexis T. Bell*[a]

Supported Co is an effective catalyst for the Fischer–Tropsch synthesis of various hydrocarbon products that can be converted to diesel. Recent studies have shown that the formation of methane can be suppressed and the formation of C_{5+} products enhanced by promoting Co with Mn. Because the activity and product selectivity of Co-based catalysts are dependent on the size of Co nanoparticles and the extent of Co promotion by Mn, it is desirable to understand these effects by investigating the performance of Co nanoparticles with well-defined size and elemental composition. The present study was undertaken with the aim of producing well-defined nanoparticles of Co and Co–Mn and then supporting them on silica. Co and Co–Mn particles were synthesized through the polyol reduction of Co and Mn acetylacetonates. By controlling synthesis conditions, Co particles with diameters of 7–10 nm and similarly sized Co–Mn (Mn/Co = 0.1) particles were prepared. XRD and elemental mapping with scanning TEM-energy-dispersive X-ray

spectroscopy and scanning TEM-electron energy loss spectroscopy studies suggested that most of the Mn species was associated with the Co particles. Ex situ prepared Co and Co–Mn nanoparticles were first supported on silica and then investigated for the catalytic activity for the Fischer–Tropsch synthesis. The turnover frequencies and product distributions obtained with silica-supported Co and Co–Mn nanoparticles were similar to those obtained with catalysts prepared by using the conventional incipient wetness impregnation method. However, the rate of CO consumption per mass of Co was much lower for the catalysts produced by supporting ex situ prepared nanoparticles. This effect was attributed to the sintering of the nanoparticles during their calcination and reduction. Magnetic interactions among nanoparticles during their immobilization and thermal pretreatment were identified as the primary cause of sintering.

Introduction

Co-based catalysts have been investigated extensively for the production of diesel by using Fischer–Tropsch synthesis (FTS).[1] In contrast to Fe-based catalysts for FTS, Co-based catalysts produce water as the primary O-containing byproduct and demonstrate a high probability for hydrocarbon chain growth than for termination. Because the primary final product of FTS is diesel in most instances, it is desirable to minimize the formation of methane and other light hydrocarbons (C_2–C_5) and to maximize the formation of C_{5+} products. Extensive research has shown that these goals can be achieved through the use of appropriate supports (e.g., TiO_2) and promoter elements (e.g., Mn, Zr, or La). The promotion of Co by Mn has been a subject of particular interest because it results in a lower selectivity toward methane and a higher selectivity toward C_{5+} products than those observed for unpromoted Co catalysts.[2–5] Our recent work demonstrates that promotion by Mn can decrease methane selectivity by approximately 50% under a wide range of operating conditions and, at high pressures

and CO conversions, result in a C_{5+} selectivity of approximately 90%.[6]

Although the beneficial effects of Mn on Co-based catalysts for FTS have been identified, the manner in which Mn interacts with Co and the oxidation state of Mn remain the subject of ongoing discussion. The conventional route for the preparation of Mn-promoted Co involves incipient wetness impregnation (IWI) of a support material (e.g., SiO_2, Al_2O_3, or TiO_2) with an aqueous solution of reducible metal salts [e.g., $Co(NO_3)_2$ and $Mn(CH_3COO)_2$]. These precursors are then decomposed through calcination and subsequently reduced to form the active catalyst. Although XRD and TEM studies indicate that Co is present as metal nanoparticles with diameters in the range of 5–20 nm, the form of Mn is much less well defined. Existing scanning TEM-electron energy loss spectroscopy (STEM-EELS) studies suggest that Mn is present in Co–Mn spinels or in MnO_x particles decorating the Co nanoparticle surfaces and dispersed separately on the support. Therefore, identifying the mechanistic role of Mn has not been possible with conventionally prepared Mn-promoted Co catalysts.[2]

Synthesizing nanoparticles ex situ and then immobilizing them on the support material can yield well-defined model catalysts that avoid the complications of particle size and composition heterogeneity that are common with conventionally prepared catalysts.[7] The present study was undertaken with

[a] Dr. S. Werner, G. R. Johnson, Prof. A. T. Bell
Department of Chemical and Biomolecular Engineering
University of California
107 Gilman Hall, Berkeley, CA 94720-1462 (USA)
E-mail: bell@cchem.berkeley.edu

the aim of producing well-defined nanoparticles of Co and Mn-promoted Co and then supporting them on silica. Co and Co–Mn nanoparticles were produced by using a modified polyol reduction process leading to the formation of particles with mean diameters in the range of 7–10 nm. These particles were characterized by high-resolution TEM and STEM and then supported on silica for investigating their activity and selectivity for FTS.

Results and Discussion

Synthesis of Co nanoparticles by the polyol process

The TEM images of three batches of nanoparticles synthesized under identical conditions along with the corresponding particle size distributions are shown in Figure 1. The combined par-
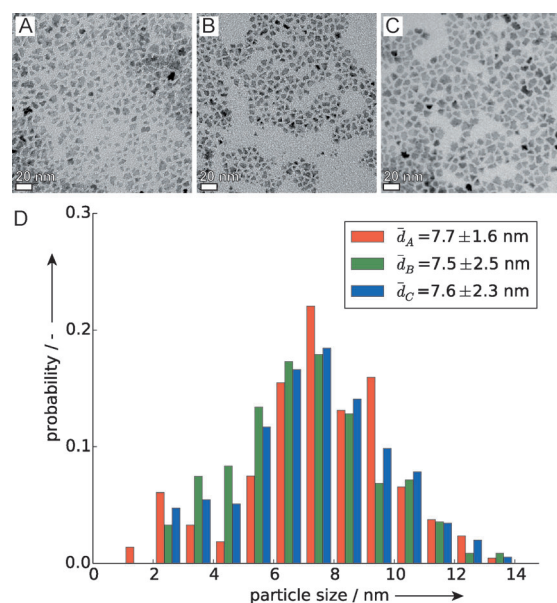

Figure 1. Reproducibility of the polyol synthesis process. A–C) TEM images of three batches of nanoparticles synthesized by using 0.25 mmol of cobalt(II) acetylacetonate, 0.9 mmol of oleylamine, 0.75 mmol of 1,2-hexadecanediol at 280 °C (heating rate: 10 °C min^{-1}); the mixture was held at this temperature for 15 min (Table 1, entry 1). Scale bar = 20 nm. D) Resulting particle size distribution using the area equivalent diameter (circularity ≈ 0.7).

ticle size distribution was monomodal, with a mean of 7.6 nm and 1σ deviation of ±2.1 nm and a circularity of approximately 0.7. The individual nanoparticles were platelike, mostly with a pentagonal shape (Figure 1 a–c), which is in agreement with previous findings.[8, 9] The nanoparticles in the solution had a greenish color when the mixture was kept under inert conditions (under nitrogen). Upon exposure to air, the greenish color changed quickly to brown and then gray, presumably owing to the oxidation of Co to cobalt oxides. The crystal structure of the air-exposed nanoparticles was identified as a mixture of cobalt(II) oxide and cobalt(II, III) oxide spinel (see Supporting Information S1). The results of high-resolution electron microscopy revealed a highly crystalline structure (see

Supporting Information S2), which is in agreement with the results of Cha et al.[8]

Decreasing the amount of the precursor by half to 0.125 mmol decreased the mean particle size to 6.9 nm (Table 1, entry 2); doubling the amount of the precursor to 0.5 mmol increased the mean particle size to 13.0 nm (Table 1, entry 3). The overall shape of the particles and the spread of the particle size distribution remained constant. These results indicated that within the examined range, the amount of the precursor used in the synthesis directly affected the resulting particle size, which enables the tuning of the particle size to ranges useful for studying FTS reaction kinetics.[10]

Particle sizes were more sensitive to the amount of capping agent used than to the amount of precursor. The use of just half the usual amount of the capping agent produced mostly large flowerlike structures in the size range of several micrometers without evidence of the formation of pentagonal nanoparticles. In this case, the nanoparticles could not be stabilized in the solution, which resulted in aggregation and restructuring as a consequence of secondary ripening processes (e.g., Ostwald ripening).[8, 11] Doubling the amount of the capping agent decreased the final particle size to 5.8 nm (Table 1, entry 5). This finding is consistent with the concept that capping agents enable colloidal stability and inhibit aggregation, which limits particle growth.[12–14]

A decrease in the heating rate from 10 to 5 K min^{-1} led to a decrease in the mean particle size to 5.2 nm (Table 1, entries 1 and 8). The slower temperature ramp may have decreased the rate at which the Co precursors reduced and allowed time for more nuclei to form.[15] A greater number of nuclei in the synthesis broth would account for the smaller particle sizes.

The reboiling time is believed to primarily affect the degree of Ostwald ripening and aggregation. Thus, decreasing the reboiling time to 0 min (quenching immediately after the heating ramp) resulted in smaller particles whereas increasing the reboiling time from 15 to 30 min increased the particle size from 7.5 to 10.5 nm (Table 1, entries 1 and 10).

This exploration of the parameter space indicated that the polyol synthesis process can be adjusted to achieve a wide range of particle sizes, including sizes that give suitable particle dispersion and turnover frequencies for FTS.[10, 16]

Synthesis of mixed Co–Mn nanoparticles

The polyol synthesis process was used to prepare well-defined nanoparticles containing both Co and Mn. Owing to the low standard reduction potential of Mn^{II} precursors, −1.18 V, which is below the reduction potential of typical reducing agents such as ethylene glycol (−0.8 V),[17] 1,2-hexadecanediol (−0.403 V),[7] and hydrazine (−1.16 V),[18] Mn^{II} precursors cannot be easily precipitated to its metallic form. However, manganese(III) precursors demonstrate a higher reduction potential (0.35 V) and are thus significantly more reducible, which offers a more promising choice for the polyol process.[19] As a result, we used manganese(III) acetylacetonate as the manganese precursor for our study.

The precipitation of manganese(III) acetylacetonate alone under the reaction conditions used for the preparation of Co particles resulted in the formation of large flowerlike aggregates with diameters of several hundred micrometers. Coprecipitation from a 1:10 Mn/Co mixture of Mn and Co precursors under standard reaction conditions (Table 1, entry 1) produced a bimodal particle size distribution with one maximum at (2.5 ± 1.1) nm and another maximum at (7.8 ± 1.9) nm (Figure 2). The resulting particles were pentagonal in shape, with a circularity of approximately 0.63. An XRD pattern of the purified nanoparticles (Figure 2c) demonstrated a pattern consistent with that found for $Co_{0.9}Mn_{0.1}O$ (ICDD pattern #78-

1991).[20] The macroscopic composition of the nanoparticles determined from ICP analysis was 9.2% Mn and 90.8% Co, which indicated a high stoichiometric yield of the bimetallic particles.

To confirm the microscopic composition of the synthesized particles, energy-filtered TEM and STEM-energy-dispersive X-ray spectroscopy (STEM-EDS) were used. The energy-filtered TEM images (Figure 3a) revealed that Co and Mn are uniformly

Figure 3. Elemental maps of unsupported Co–Mn nanoparticles. A) High-resolution TEM image (gray scale) with superimposed energy-filtered TEM images for Co (green) and Mn (red). B) STEM-EDS (count-map) image of nanoparticles used for elemental analysis.
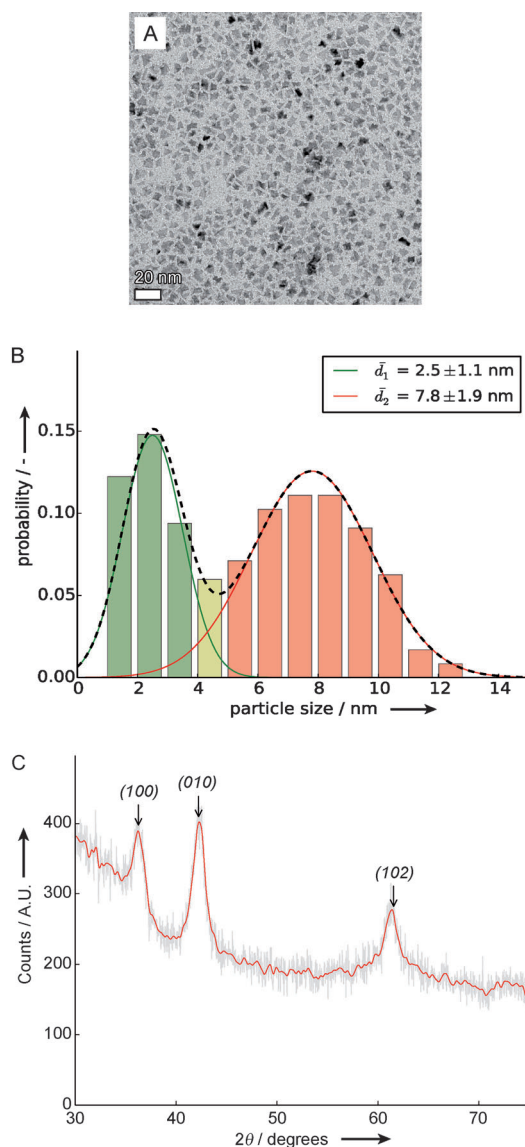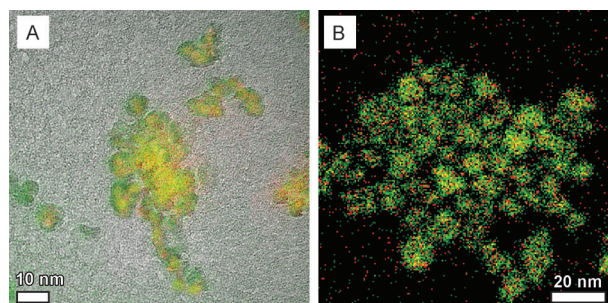

Figure 2. Synthesis of mixed Co–Mn nanoparticles by using the polyol process. A) TEM image of particles synthesized by using 0.25 mmol of cobalt(II) acetylacetonate, 0.025 mmol of manganese(III) acetylacetonate, 0.9 mmol of oleylamine, 0.75 mmol of 1,2-hexadecanediol at 280 °C (heating rate: 10 °C min^{-1}); the mixture was held at this temperature for 15 min. B) Bimodal particle size distribution using the area equivalent diameter (circularity ≈ 0.63). The dashed line indicates the sum of fitted normal distributions for the small (red) and large (green) particles. C) XRD pattern of this material, indicating peak positions of the ICDD pattern #78-1991.

distributed within the larger particles. No evidence for the formation of separate MnO_x particles was found; however, the smaller particles of the bimodal size distribution were found to contain very little Mn. Because energy-filtered TEM provides only a qualitative analysis of the elemental composition, STEM-EDS was used to obtain a quantitative estimate of the Mn and Co contents of the large and small particles. The quantification of the acquired count maps revealed that small particles contained lower Mn concentrations, in the range of the detection limit (2 ± 1) at% Mn, than did larger particles, which contained (18 ± 1) at% Mn. The particle size distribution data revealed that 36% of all particles were in the Co-rich, small particle fraction. By using a weighted average, it can be calculated that approximately 13% of the Co particles existed in the small particle fraction. Thus, 99% of the Mn particles existed in the large particle fraction. The overall elemental composition of the particles calculated by using the particle size distribution and EDS compositions was 9.4% Mn and 90.6% Co, which was in agreement with the ICP results. The possibility of such Co–Mn solid mixtures has previously been reported for macroscopic systems;[21] however, mixtures within prepared nanoparticles have not been reported to our knowledge.

The observed bimodal distribution can be rationalized by considering the findings of Sun et al., who prepared Pt–Ag nanoparticles by using the polyol process.[22] These researchers observed a bimodal size distribution for their bimetallic nanoparticles that was attributed to the interplay between homogeneous and heterogeneous nucleation processes. Because of its higher reduction potential, manganese(III) acetylacetonate is expected to undergo reduction before cobalt(II) acetylacetonate with the heating of the synthesis broth, which could lead to the formation of Mn nanoparticles that could serve as nuclei for Co precipitation. This reaction pathway could be the

growth mechanism responsible for the formation of the larger Mn-rich nanoparticles because the deposition of Co on the existing Mn nanoparticles would be facile relative to the formation of Co nuclei. However, the homogeneous nucleation of Co could still occur, which would lead to smaller Mn-poor nanoparticles.

The EELS analysis of the purified nanoparticles revealed that Mn was present in the +2 and +3 oxidation states because the Mn L_3 peak, with an edge energy of 642.6 eV, matches that reported for Mn_3O_4 (see Supporting Information S3).[23] This finding is consistent with the previously stated observation that Mn oxidizes easily and was most likely present in an oxidized state.

Catalytic testing of the immobilized nanoparticles

The catalytic performance of silica-supported, ex situ prepared Co and Mn-promoted Co nanoparticle catalysts was compared with that of similar catalysts prepared by using the IWI method. As shown in Figure 4a, the rates of CO consumption per mass of Co for the nanoparticle catalysts were significantly lower than those of the catalysts prepared by using the IWI method. However, methane and C_{5+} selectivities were comparable for catalysts prepared by both methods. In both cases, a decrease in methane selectivity and an increase in C_{5+} selectivity were observed if the catalysts contained Mn.

Various explanations for the differences in the activities of silica-supported, ex situ prepared nanoparticle catalysts and the catalysts prepared by using the IWI method were considered. This effort led to the conclusion that although the freshly prepared unsupported nanoparticles and the nanoparticles within the catalysts prepared by using the IWI method were of similar size, the ex situ prepared nanoparticles supported on silica sintered upon pretreatment. The following evidence supports this conclusion. As discussed above, freshly prepared Co and Co–Mn nanoparticles had a mean size of approximately 7.5 nm (dispersion of 13%); however, the TEM images
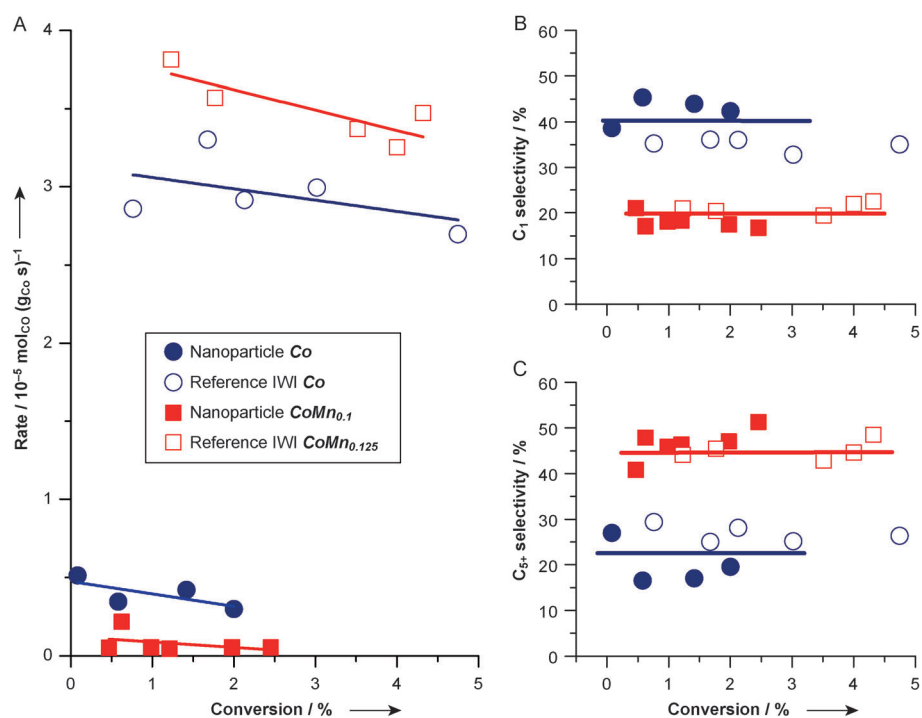

Figure 4. Catalytic data of nanoparticle catalysts (●, ■) in comparison to the catalysts prepared by using the IWI method (○, □) for both unpromoted (●, ○) and Mn-promoted (■, □) types. A) CO consumption rates per mass of Co. B) Methane selectivity. C) C_{5+} selectivity. Data obtained at $T=220\,°C$, $P_{total}=1$ atm, $H_2/CO=2$, $V_{total}=50–150$ mL min^{-1}, $m_{catalyst}=0.25$ g.

acquired after these particles had been dispersed on silica and calcined showed a larger mean particle size of 200 ± 100 nm [dispersion of (0.5 ± 0.2)%]. An example of these large sintered particles is shown in Figure 5b. In comparison, Figure 5c shows that the mean particle diameter of the supported Co nanoparticles prepared by using the IWI method was 8.5 nm (dispersion of 11%). Additional larger-scale STEM-high-angle annular dark-field (STEM-HAADF) and EDS maps are provided in Supporting Information S5.

For the ex situ prepared nanoparticle catalysts, the activity of Co catalysts was higher than that of Mn-promoted catalysts; however, this trend was reversed for the catalysts prepared by using the IWI method. We can rationalize this finding by considering the effective loading of Mn on the catalyst surface for
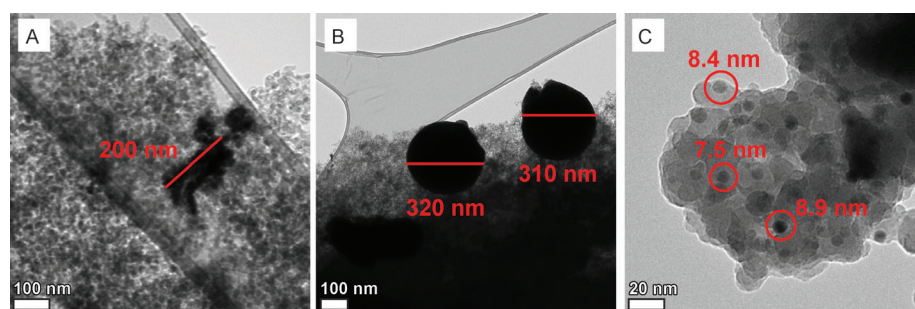

Figure 5. Change in the nanoparticle morphology due to heat treatment as observed by TEM. A) Co nanoparticles after immobilization on silica using hexane and 15 min ultrasonic treatment. B) Sintered nanoparticles after air calcination treatment at 200 °C. C) Reference catalysts prepared by using the IWI method after reduction at 450 °C.

the two Mn-promoted catalysts. Owing to its lower surface free energy relative to that of Co,[24] Mn would be expected to migrate toward the surface of the reduced nanoparticles. Evidence for this phenomenon was visible in the STEM-EDS maps of the nanoparticles, which showed an enrichment of Mn in the surface of the sintered particles (see Supporting Information S6). Although the bulk Mn loading of the ex situ prepared nanoparticle catalyst was the same as that of the catalyst prepared by using the IWI method (Mn/Co=0.1), the Mn/Co ratio on the particle surfaces could differ markedly because of the considerable differences in the mean particle size. In the limiting case of Mn being located entirely on the particle surfaces, the surface concentration of Mn would be approximately 20 times greater for the ex situ prepared nanoparticle catalyst than that for the catalyst prepared by using the IWI method. Our previous work established that the catalytic activity per mass of Co for Mn-promoted catalysts prepared by using the IWI method was lower than that for unpromoted catalysts prepared by using the IWI method when Mn loading was greater than Mn/Co=0.25, which was most likely due to the coverage of the Co metal surface by Mn species.[6] The ex situ prepared nanoparticle catalyst could have a surface composition similar to that of a catalyst prepared by using the IWI method with Mn/Co≈2, which would be consistent with the fact that the Mn-promoted, ex situ prepared nanoparticle catalyst is less active than the unpromoted catalyst. The observation of similar product selectivities for Mn-promoted catalysts in this study is consistent with our previous finding that the selectivity is not affected by Mn loading above Mn/Co=0.05.

Particle sintering and evidence of magnetic interactions

Experiments were performed to understand the cause of the decrease in Co surface area upon dispersion and pretreatment of ex situ prepared nanoparticles. The TEM images of silica-supported Co and Co–Mn catalysts acquired before calcination revealed the evidence of particle aggregate formation (Figure 5a and see Supporting Information S5). The size of these aggregates was of the order of 100–300 nm. This behavior was found to be independent of the solvent used (hexane, cyclohexane, toluene, and ethanol) to suspend the nanoparticles; the amount of the solvent used; the use of ultrasonication during drying; and whether the solvent was removed by air drying, vacuum drying, or freeze drying. The TEM images of unsupported Co nanoparticles on lacey carbon TEM grids also revealed signs of aggregation owing to self-assembly. Previous observations of Co nanoparticles have indicated that the formation of such superstructures can be attributed to magnetic interactions of individual nanoparticles.[25, 26]

The results of XRD analysis (Supporting Information S1) revealed that the freshly prepared nanoparticles investigated herein contained a mixture of Co and CoO/Co$_3$O$_4$. Co is ferromagnetic, and the paramagnetic nature of the oxides can amplify the magnetism. To quantify this effect, we performed magnetic polarization measurements of the magnetic moment of air-dried and calcined catalysts in a superconducting quantum interference device (SQUID). The air-dried catalyst showed

a saturation signal at both positive and negative fields with minimal hysteresis (Figure 6). Although this signal was fairly noisy because the particles were immobilized and the sample weight was low, the overall observation was consistent with small magnetic particles containing small magnetic domains caused by Co. After the catalyst was calcined, reduced, and
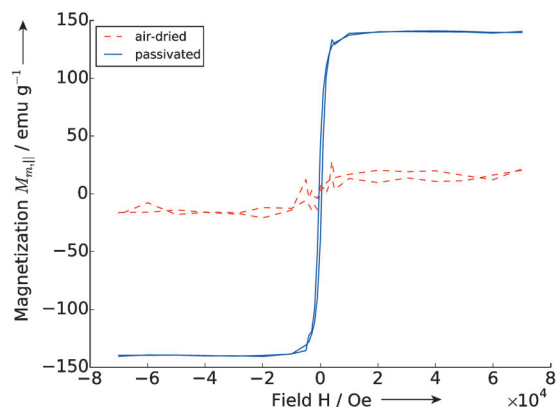
Figure 6. Magnetic moments of silica-supported nanoparticles after drying in air at room temperature and after calcination, reduction, and passivation. Measured with a SQUID using field strength between −7 and 7 T on 15 mg of the sample. Values are normalized by Co loading with background subtraction.

subsequently passivated (using 500 ppm O$_2$/He), the magnetic moment demonstrated saturation at both positive and negative fields. A saturation magnetization of approximately 150 Am^2 kg^{-1} was measured, which was in the same range as values reported by Kim et al. for unsupported Co nanoparticles.[27] The small hysteresis found in the range of ±0.2 T has also been reported for Co and cobalt oxides.[28]

Martínez and Prieto found that the dispersion of cobalt oxide nanoparticles on the silica support could be facilitated by silylating the support material.[29] This treatment increases the hydrophobicity of the support surface, which could improve chemical compatibility with the nonpolar capping agents that surround the nanoparticles. To explore this effect, we immobilized Co nanoparticles on silylated silica (see the Experimental Section); however, this technique did not lead to any abatement in nanoparticle agglomeration. A key difference between the present study and that of Martínez and Prieto was the use of hydrazine as a reducing agent, which was not strong enough to reduce Co completely to a metallic state. Thus, their catalyst samples probably did not demonstrate the same degree of ferromagnetism as did ours. For nanoparticles prepared according to our protocols, the silylation of the support was insufficient to overcome the magnetic forces between these nanoparticles.

A previous study by Somodi et al. involving immobilized oleylamine-capped Pt$_3$In nanoparticles on silica did not find signs of particle agglomeration.[30] The same support material and nanoparticle capping agents were used in our study. Because the intermolecular interactions between the capping agent and the silica support were the same in both studies using Pt$_3$In and Co nanoparticles, it is logical to attribute the

absence and presence of nanoparticle agglomeration in the respective studies to the differences in nanoparticle composition. Specifically, the PtIn3 nanoparticles were nonmagnetic and the Co and Co–Mn particles were magnetic. Taken together, our observations suggest that the nanoparticles aggregate during the immobilization process and the impregnation solvent evaporates owing to the magnetic nature of the Co and cobalt oxide. Subsequent calcination and reduction at elevated temperature lead to the sintering of supported particles, which results in the formation of large, low-surface area particles.

In an attempt to mitigate the magnetic attraction between particles, we prepared core–shell particles with Pt seeds by using protocols from our work with core–shell Pt–In nanoparticles.[30] Although Co–Pt nanoparticles with the desired core–shell morphology were prepared (see Supporting Information S7), this approach did not improve the dispersion of supported nanoparticles after pretreatment. Notably, in the absence of magnetic interactions, the ex situ prepared nanoparticles can be supported without aggregation during drying, calcination, and reduction, as observed in our recent work on MgO-supported Pt and Pt–Sn nanoparticles.[31] At the time of writing this article, Rothenberg et al. had developed a different approach to overcome this limitation by placing nanosized alumina as spacers between individual Co–Fe core–shell particles.[32] Finally, Park et al. reported the synthesis and dispersion of cobalt oxide nanoparticles on the alumina support to yield a catalyst active for FTS. However, our attempts to reproduce their work resulted in micrometer-scale aggregates of Co (see Supporting Information S8).[33]

Conclusions

The effect of synthesis parameters on the preparation of Co and Co–Mn nanoparticles by using the polyol process was investigated. The Co particles produced by this method showed a monomodal particle size distribution that was tunable from 5 to 13 nm by changing the concentration of precursor, the reboiling/ripening time, and the heating rate. Co–Mn nanoparticles were prepared in a similar manner. TEM characterization revealed that the Co–Mn particles demonstrated a bimodal size distribution, containing small particles that were Mn-poor and larger particles that were Mn-rich. These particle size distributions and composition trends were attributed to Co reducing after Mn such that most Co deposited on the existing Mn nanoparticles while a small portion also formed new Co nuclei.

The catalytic activity per mass of Co was lower for the ex situ prepared nanoparticle catalysts than for catalysts prepared by using the incipient wetness impregnation method. However, the turnover frequencies and product selectivities for the two types of catalysts, as well as the effect of including Mn, were comparable. The discrepancy between the specific activities for the two types of catalysts was attributed to the sintering of ex situ prepared nanoparticles during their immobilization and pretreatment, which led to a significant increase in particle size and decrease in catalytically active surface area. The aggregation of the nanoparticles in the immobilization step was probably due to the ferromagnetic nature of Co.

These agglomerated nanoparticles then sintered after thermal treatment.

Experimental Section

Synthesis and purification of Co and Co–Mn nanoparticles

On the basis of the synthesis method published by Cha et al., we prepared batches of Co nanoparticles.[8] In a typical synthesis of Co nanoparticles, cobalt(II) acetylacetonate (0.25 mmol; 97% purity) was combined with 1,2-hexadecanediol (0.75 mmol; 99% purity) and oleylamine in dioctylether (10 mL) in a 50 mL three-necked flask. To prepare Co–Mn nanoparticles, manganese(III) acetylacetonate (0.025 mmol; 97% purity) was also included in the synthesis mixture. 1,2-Hexadecanediol and oleylamine served as the reducing agent and surface capping agent, respectively. All chemicals were purchased from Sigma–Aldrich and used without further purification.

The flask was equipped with a thermocouple in a quartz sleeve and placed within a heating mantle to control the temperature of the solution. A water-cooled condenser connected to a Schlenk line ensured the solution was heated at reflux temperature during synthesis. The mixture was stirred continuously with a magnetic stirrer. After stirring at RT for 5 min and flushing the system with nitrogen to achieve an inert atmosphere, the mixture was heated to 280 °C (heating rate: 10 °C min^{-1}). After holding at this temperature for 15 min, the mixture was cooled to RT by removing the heating mantle.

After validation of the synthesis method, systematic parameter variation was performed to explore the effects of the precursor concentration, capping agent concentration, reducing agent concentration, heating rate, and reboiling time. A catalog of synthesis parameters and the resulting mean nanoparticle sizes is given in Table 1. Each set of synthesis parameters was repeated several times to ensure reproducibility. The "reference case" synthesis parameters, which were discussed previously in this section, correspond to entry 1 in the table.

To isolate the synthesized nanoparticles, the sol (2 mL) was combined with absolute ethanol (4 mL; ACS grade) and centrifuged for 15 min. After discarding the supernatant, the black precipitate was redispersed with hexane (200 μL) and the washing process was repeated.

Immobilization of nanoparticles on catalyst supports

The Co or Co–Mn nanoparticles were supported on silica in the following manner: silica gel (0.2 g; CS-2129 silica support, PQ Corporation, USA) was placed in a test tube and then mixed with a suspension (0.5 mL) of the purified nanoparticles in hexane. The resulting material was air dried overnight. To remove the capping agent, the catalyst was air calcined at 200 °C (see Supporting Information S4). The bulk catalyst composition was determined from inductively coupled plasma (ICP) optical emission spectrometry analysis (Galbraith Laboratories, USA), which was (5 ± 1) wt% Co. The reference catalysts were prepared by using the IWI method with cobalt(II) nitrate and manganese(II) acetate precursors, as described previously.[7] These catalysts had Co loadings of 10 wt%.

The nanoparticles were also supported on silylated silica gel treated by using a method reported by Sindorf and Macial.[34] In a typical synthesis, silica gel (1 g) was dispersed in toluene (50 mL) in a three-necked flask and heated to 95 °C under nitrogen. After the

Table 1. Varied parameters for the synthesis of Co nanoparticles by using the polyol process.						
Entry	Amount [mmol]			Heating rate [K min^{-1}][d]	Reboil time [min]	Mean size [nm][e]
	Precursor[a]	Capping agent[b]	Reducing agent[c]			
1	0.25	0.9	0.75	10	15	7.5
2	0.125	0.9	0.75	10	15	6.9
3	0.5	0.9	0.75	10	15	13.0
4	0.25	0.45	0.75	10	15	–[f]
5	0.25	1.35	0.75	10	15	5.8
6	0.25	0.9	0.375	10	15	9.1
7	0.25	0.9	1.5	10	15	5.3
8	0.25	0.9	0.75	5	15	5.2
9	0.25	0.9	0.75	7.5	15	6.6
10	0.25	0.9	0.75	10	0	6.0
11	0.25	0.9	0.75	10	30	10.5

[a] Cobalt(II) acetylacetonate; [b] Oleylamine; [c] 1,2-Hexadecanediol; [d] Final temperature = 280 °C; [e] Area-derived mean particle size determined by counting > 1000 individual particles in multiple TEM images; [f] No stable nanoparticles were formed.

edge with pre-edge energies of 690 ± 15 and 745 ± 15 eV against the post-edge energy of 780 ± 15 eV with a 20 s exposure. The Mn-sensitive images were acquired at the L$_{2,3}$ edge with pre-edge energies at 590 ± 15 and 610 ± 15 eV against the post-edge energy of 640 ± 15 eV with a 30 s exposure. The same instrument was used to record the EELS spectra of the selected nanoparticles.

Quantitative elemental maps were recorded with a custom-modified FEI Titan electron microscope equipped with a Bruker Nano EDS detector at the National Center for Electron Microscopy. Maps were recorded at 80 kV at a beam current of 0.5 nA and a convergence angle of 10 mrad in the STEM mode after selecting a region of the sample by using the HAADF image. All EDS maps used a pixel dwell time of 150 μs with averaging of at least 100 frames with drift compensation. Bruker ESPRIT software package was used to quantify the maps by fitting and subtracting the Bremsstrahlung background using regions without peaks. After this step, the Co K$_\alpha$ emission peak at 6.93 keV and the Mn K$_\alpha$ peak at 5.89 keV were integrated and converted to atomic compositions by using Cliff–Lorimer factors.[36]

Silica-supported nanoparticle catalysts were prepared by milling the catalyst (5 mg) in a mortar for 30 s. The fine powder was then dispersed in hexane (1 mL) and ultrasonicated for 60 s before the suspension (5 μL) was drop-casted on a lacey carbon grid (LC300-Cu, Electron Microscopy Sciences). These catalysts were characterized by using bright-field TEM (FEI Tecnai T12) and STEM-HAADF (FEI Tecnai T20). For the STEM-HAADF images, a convergence angle of 12 mrad was maintained by using a spot size of 8 in conjunction with a C$_2$ aperture of 100 μm at 200 kV.

injection of methyltrimethoxysilane (0.41 g; Sigma–Aldrich, USA, 98 %), the suspension was heated at reflux for 10 h and then cooled; then, the suspension was washed repeatedly with toluene and dried in a vacuum oven at 40 °C.

Electron microscopy

The samples for TEM were prepared as follows: The redispersed nanoparticle suspension (5 μL) was diluted in hexane (1 mL) and ultrasonicated for 5 min. Then, this suspension (5 μL) was drop-casted on an ultrathin carbon film mounted on a holey carbon film supported on a copper TEM grid (Ted Pella #1824). The prepared TEM grids were then dried in a vacuum oven at 60 °C and 0.1 bar (absolute; 1 bar = 100 kPa) for 5 min to remove the solvent.

The nanoparticles were characterized with an FEI Tecnai T12 transmission electron microscope to determine particle size distributions. Particle sizes were determined by analyzing multiple TEM images of the sample acquired at different positions on the grids to confirm the uniformity of the sample. To ensure accurate particle size distributions, more than 1000 particles were counted by using the image analysis software ImageJ (64-bit).[35] The particle size d_p described herein was determined by using the software and was based on the particle projected area A_p [see Eq. (1)]. Additional parameters such as the Feret diameter and the circularity were calculated as well.

$$d_p = 2\sqrt{\frac{A_p}{\pi}} \qquad (1)$$

Quantitative elemental maps were obtained with an FEI Tecnai T20 transmission electron microscope at the National Center for Electron Microscopy at Lawrence Berkeley National Laboratory. Images were acquired at 200 kV with a C$_2$ aperture of 300 μm and an objective aperture of 60 μm using a spot size of 3 at a beam current of 0.5 nA. The Gatan Imaging Filter was aligned to the zero loss peak and subsequently calibrated using the carbon K-edge at 284.3 eV because carbon was present in the support grid. The Co-sensitive energy-filtered STEM images were acquired at the L$_{2,3}$

XRD

A Siemens D500 X-ray diffractometer at the University of California, Berkeley, was used to determine the crystal structure. To acquire XRD patterns of the fresh nanoparticles, the concentrated, washed nanoparticle suspension (100 μL) was drop-casted on a standard XRD holder. The dry free flowing catalyst powder was characterized by XRD by mixing silica-supported catalysts (100 mg) with Vaseline and smearing it on a standard XRD holder.

Catalytic testing

The catalytic activity was measured in a flow microreactor as described previously.[6] For these tests, silica-supported catalysts (250 mg) were placed in a quartz glass reactor. The catalysts were calcined in 20 % O/He at 200 °C for 1 h (heating rate: 5 °C min^{-1}) and reduced in pure H$_2$ gas at 450 °C for 1 h (heating rate: 5 °C min^{-1}). The activity data were collected at 220 °C, 1 atm (1 atm = 101.3 kPa), and H$_2$/CO = 2 (Table 2). Conversion was maintained at ≤ 5 % to ensure differential behavior, and volumetric flow rates were varied so that the measured reaction rates could be extrapolated to 0 % conversion. The effluent products were analyzed with an Agilent 6890N gas chromatograph equipped with a Porapak Q packed column connected to a thermal conductivity detector to determine CO consumption and to an HP-1 column connected to a flame ionization detector to analyze hydrocarbons.

Acknowledgements

Table 2. Catalytic results for the Fischer–Tropsch synthesis comparing Co nanoparticle catalysts with the catalysts prepared by using the IWI method.[a]

Catalyst	d_p[b] [nm]	Dispersion N_{surf}/N_{total}	$-r_{CO}$[c] $[10^{-5}\,mol_{CO}\,g_{Co}^{-1}\,s^{-1}]$	Turnover frequency $[s^{-1}]$
Nanoparticle model catalyst	200 ± 100	$0.5 \pm 0.2\%$	0.4 ± 0.1	0.05 ± 0.03
IWI reference catalyst	8.5 ± 2.0	$11 \pm 3\%$	3.0 ± 0.2	0.016 ± 0.005

[a] Reaction conditions: $T = 220\,°C$, $P_{total} = 1$ atm, $H_2/CO = 2$, $V_{total} = 50$–$150\,mL\,min^{-1}$. Activities were extrapolated to 0% conversion; [b] Analysis of 100 individual particles; [c] Extrapolated to 0% conversion.

[1] A. Y. Khodakov, W. Chu, P. Fongarland, *Chem. Rev.* **2007**, *107*, 1692–1744.

[2] F. Morales, D. Grandjean, F. M. F. de Groot, O. Stephan, B. M. Weckhuysen, *Phys. Chem. Chem. Phys.* **2005**, *7*, 568–572.

[3] F. Morales, B. M. Weckhuysen, *Catalysis* **2006**, *19*, 1–40.

[4] F. Morales, F. M. de Groot, O. L. Gijzeman, A. Mens, O. Stephan, B. M. Weckhuysen, *J. Catal.* **2005**, *230*, 301–308.

[5] J. P. den Breejen, A. M. Frey, J. Yang, A. Holmen, M. M. van Schooneveld, F. M. F. de Groot, O. Stephan, J. H. Bitter, K. P. de Jong, *Top. Catal.* **2011**, *54*, 768–777.

[6] A. Dinse, M. Aigner, M. Ulbrich, G. R. Johnson, A. T. Bell, *J. Catal.* **2012**, *288*, 104–114.

[7] H. Bönnemann, G. Braun, W. Brijoux, R. Brinkmann, A. S. Tilling, K. Seevogel, K. Siepen, *J. Organomet. Chem.* **1996**, *520*, 143–162.

[8] S. I. Cha, C. B. Mo, K. T. Kim, S. H. Hong, *J. Mater. Res.* **2005**, *20*, 2148–2153.

[9] K. Simeonidis, S. Mourdikoudis, A. Vilalta-Clemente, I. Tsioussis, M. Angelakeris, O. Kalogirou, *Physics of Advanced Materials Winter School*, **2008**, 1–8.

[10] E. Iglesia, *Appl. Catal. A* **1997**, *161*, 59–78.

[11] T. Hyeon, Y. Chung, J. Park, S. S. Lee, Y.-W. Kim, B. H. Park, *J. Phys. Chem. B* **2002**, *106*, 6831–6833.

[12] K. An, G. A. Somorjai, *ChemCatChem* **2012**, *4*, 1512–1524.

[13] K. An, S. Alayoglu, T. Ewers, G. A. Somorjai, *J. Colloid Interface Sci.* **2012**, *373*, 1–13.

[14] S. Gubin, Y. A. Koksharov, *Inorg. Mater.* **2002**, *38*, 1085–1099.

[15] C. B. Murray, S. Sun, W. Gaschler, H. DoyLe, T. A. Betley, C. R. Kagan, *IBM J. Res. Dev.* **2001**, *45*, 47–56.

[16] A. Y. Khodakov, J.-S. Girardon, A. Griboval-Constant, A. S. Lermontov, P. A. Chernavskii, *Stud. Surf. Sci. Catal.* **2004**, *147*, 295.

[17] F. Bonet, C. Guery, D. Guyomard, R. Herrera Urbina, K. Tekaia-Elhsissen, J.-M. Tarascon, *Solid State Ionics* **1999**, *126*, 337–348.

[18] A. J. Bard, *Anal. Chem.* **1963**, *35*, 1602–1607.

[19] R. J. Joseyphus, T. Matsumoto, H. Takahashi, D. Kodama, K. Tohji, B. Jeyadevan, *J. Solid State Chem.* **2007**, *180*, 3008–3018.

[20] D. Hope, A. Cheetham, *J. Solid State Chem.* **1988**, *72*, 42–51.

[21] L. Kaufman, *CALPHAD Comput. Coupling Phase Diagrams Thermochem* **1978**, *2*, 117–146.

[22] Y. Sun, B. Mayers, T. Herricks, Y. Xia, *Nano. Lett.* **2003**, *3*, 955–960.

[23] L. Laffont, P. Gibot, *Mater. Charact.* **2010**, *61*, 1268–1273.

[24] W. R. Tyson, W. A. Miller, *Surf. Sci.* **1977**, *62*, 267–276.

[25] S. Sun, S. Anders, H. F. Hamann, J.-U. Thiele, J. Baglin, T. Thomson, E. E. Fullerton, C. Murray, B. D. Terris, *J. Am. Chem. Soc.* **2002**, *124*, 2884–2885.

[26] C. Luna, M. Morales, C. Serna, M. Vàzquez, *Mater. Sci. Eng. C* **2003**, *23*, 1129–1132.

[27] C. W. Kim, H. G. Cha, Y. H. Kim, A. P. Jadhav, E. S. Ji, D. I. Kang, Y. S. Kang, *J. Phys. Chem. C* **2009**, *113*, 5081–5086.

[28] S. Mourdikoudis, K. Simeonidis, I. Tsiaoussis, C. Dendrinou-Samara, M. Angelakeris, O. Kalogirou, *J. Nanopart. Res.* **2009**, *11*, 1477–1484.

[29] A. Martínez, G. Prieto, *Catal. Commun.* **2007**, *8*, 1479–1486.

[30] F. Somodi, S. Werner, Z. Peng, A. B. Getsoian, A. N. Mlinar, B. S. Yeo, A. T. Bell, *Langmuir* **2012**, *28*, 3345–3349.

[31] J. Wu, Z. Peng, A. T. Bell, *J. Catal.* **2014**, *311*, 161–168.

[32] V. R. Calderone, N. R. Shiju, D. Curulla-Ferré, S. Chambrey, A. Khodakov, A. Rose, J. Thiessen, A. Jess, G. Rothenberg, *Angew. Chem.* **2013**, *125*, 4493–4497; *Angew. Chem. Int. Ed.* **2013**, *52*, 4397–4401.

[33] J.-Y. Park, Y.-J. Lee, P. Karandikar, K.-W. Jun, K.-S. Ha, H.-G. Park, *Appl. Catal. A* **2012**, *411*, 15–23.

[34] D. W. Sindorf, G. E. Macial, *J. Am. Chem. Soc.* **1983**, *105*, 3767–3779.

[35] W. S. Rasband, "ImageJ," US National Institutes of Health, [Online]. Available: http://rsb.info.nih.gov/ij/. [Accessed 06 01 2014].

[36] G. Cliff, G. Lorimer, *J. Microsc.* **1975**, *103*, 1365–2818.